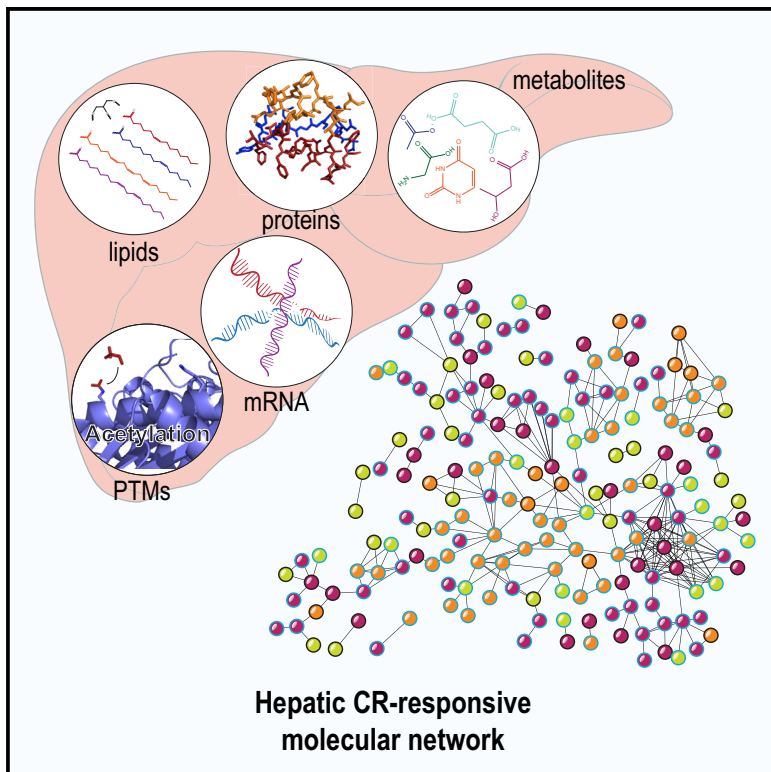


Cell Metabolism

Caloric Restriction Engages Hepatic RNA Processing Mechanisms in Rhesus Monkeys

Graphical Abstract



Authors

Timothy W. Rhoads,
Maggie S. Burhans, Vincent B. Chen, ...,
Joshua J. Coon, Ricki J. Colman,
Rozalyn M. Anderson

Correspondence

rozalyn.anderson@wisc.edu

In Brief

Rhoads et al. use multi-platform high-resolution molecular profiling to demonstrate that caloric restriction (CR) reprograms hepatic metabolism in rhesus monkeys. They identify a role for RNA processing in the mechanisms of CR and show that the CR metabolic network is subject to substantial regulation at the RNA level.

Highlights

- Caloric restriction reprograms hepatic metabolism in monkeys independently of aging
- The response to CR involves recruitment of RNA processing mechanisms
- Integrative analysis reveals a multi-pathway core CR metabolic network
- The core CR metabolic network is regulated at the level of RNA processing



Caloric Restriction Engages Hepatic RNA Processing Mechanisms in Rhesus Monkeys

Timothy W. Rhoads,^{1,11} Maggie S. Burhans,^{1,11} Vincent B. Chen,² Paul D. Hutchins,^{3,4} Matthew J.P. Rush,^{3,4} Josef P. Clark,¹ Jaime L. Stark,² Sean J. McIlwain,⁵ Hamid R. Eghbalnia,² Derek M. Pavelcik,⁶ Irene M. Ong,⁵ John M. Denu,^{7,8} John L. Markley,² Joshua J. Coon,^{3,4,8} Ricki J. Colman,⁹ and Rozalyn M. Anderson^{1,10,12,*}

¹Department of Medicine, University of Wisconsin-Madison, Madison, WI 53705, USA

²National Magnetic Resonance Facility at Madison and Department of Biochemistry, University of Wisconsin-Madison, Madison, WI 53706, USA

³Department of Chemistry, University of Wisconsin-Madison, Madison, WI 53706, USA

⁴Genome Center of Wisconsin, University of Wisconsin-Madison, Madison, WI 53706, USA

⁵Department of Biostatistics and Medical Informatics, University of Wisconsin-Madison, Madison, WI 53792, USA

⁶University of Wisconsin Biotechnology Center, University of Wisconsin-Madison, Madison, WI 53706, USA

⁷Wisconsin Institute for Discovery, University of Wisconsin-Madison, Madison, WI 53715, USA

⁸Department of Biomolecular Chemistry, University of Wisconsin-Madison, Madison, WI 53715, USA

⁹Wisconsin National Primate Research Center, University of Wisconsin-Madison, Madison, WI 53715, USA

¹⁰Geriatric Research, Education, and Clinical Center, William S. Middleton Memorial Veterans Hospital, Madison, WI 53705, USA

¹¹These authors contributed equally

¹²Lead Contact

*Correspondence: rozalyn.anderson@wisc.edu

<https://doi.org/10.1016/j.cmet.2018.01.014>

SUMMARY

Caloric restriction (CR) extends lifespan and delays the onset of age-related disorders in diverse species. Metabolic regulatory pathways have been implicated in the mechanisms of CR, but the molecular details have not been elucidated. Here, we show that CR engages RNA processing of genes associated with a highly integrated reprogramming of hepatic metabolism. We conducted molecular profiling of liver biopsies collected from adult male rhesus monkeys (*Macaca mulatta*) at baseline and after 2 years on control or CR (30% restricted) diet. Quantitation of over 20,000 molecules from the hepatic transcriptome, proteome, and metabolome indicated that metabolism and RNA processing are major features of the response to CR. Predictive models identified lipid, branched-chain amino acid, and short-chain carbon metabolic pathways, with alternate transcript use for over half of the genes in the CR network. We conclude that RNA-based mechanisms are central to the CR response and integral in metabolic reprogramming.

INTRODUCTION

The ability of caloric restriction (CR) to attenuate age-related physiological decline, reduce the incidence of age-related diseases, and extend lifespan in rodents was first reported in 1935 (McCay et al., 1935). Since then, a variety of changes accompanying CR in short-lived species have been described that may be mechanistically involved in conferring longevity benefits (Fontana and Partridge, 2015). More recently it has

become clear that the benefits of CR in lowering morbidity and mortality are translatable to primates (Mattison et al., 2017), with important implications for human aging biology (Balasubramanian et al., 2017a). The human and non-human primate (NHP) response to CR is highly congruent, with similar beneficial effects on bodyweight, body composition, glucoregulatory function, and serum indicators of cardiovascular disease risk noted in both species (Balasubramanian et al., 2017b). Rhesus monkeys share substantial genomic identity with humans (93%) (Zimin et al., 2014), along with many physiological and behavioral features (Colman and Anderson, 2011) and an increase in incidence of conditions such as cancer, diabetes, sarcopenia, and bone loss as a function of age. As such, mechanisms employed by CR to delay aging in NHPs are likely translatable to human aging and may provide targets for prevention or treatment of age-related disease vulnerability.

To date, CR mechanistic insights have been largely gleaned from short-lived species. A role for metabolism is suggested in the overt response of hepatic tissues to CR (Swindell, 2009), and CR-induced changes in hepatic gene expression (de Magalhaes et al., 2009; Plank et al., 2012; Swindell, 2008) and the hepatic metabolome have been reported (Fok et al., 2014; Jove et al., 2014). The liver plays a central role in whole-body homeostasis and metabolic health; many metabolic functions, including lipid processing and distribution, amino acid synthesis, and gluconeogenesis, are performed or controlled by the liver. To date it is not known whether hepatic molecular networks engaged by CR in mice are conserved in NHPs. Tissues from the rhesus monkey “Aging and Caloric Restriction” study present an opportunity to investigate CRs mechanisms in a model of proven efficacy (Colman et al., 2009, 2014). To interrogate the response to CR in the absence of confounding age-related changes, molecular profiling was conducted using hepatic tissue biopsies from monkeys before and after short-term (2 years) CR intervention. Data from multiple high-throughput, high-resolution techniques, including nucleotide sequencing,



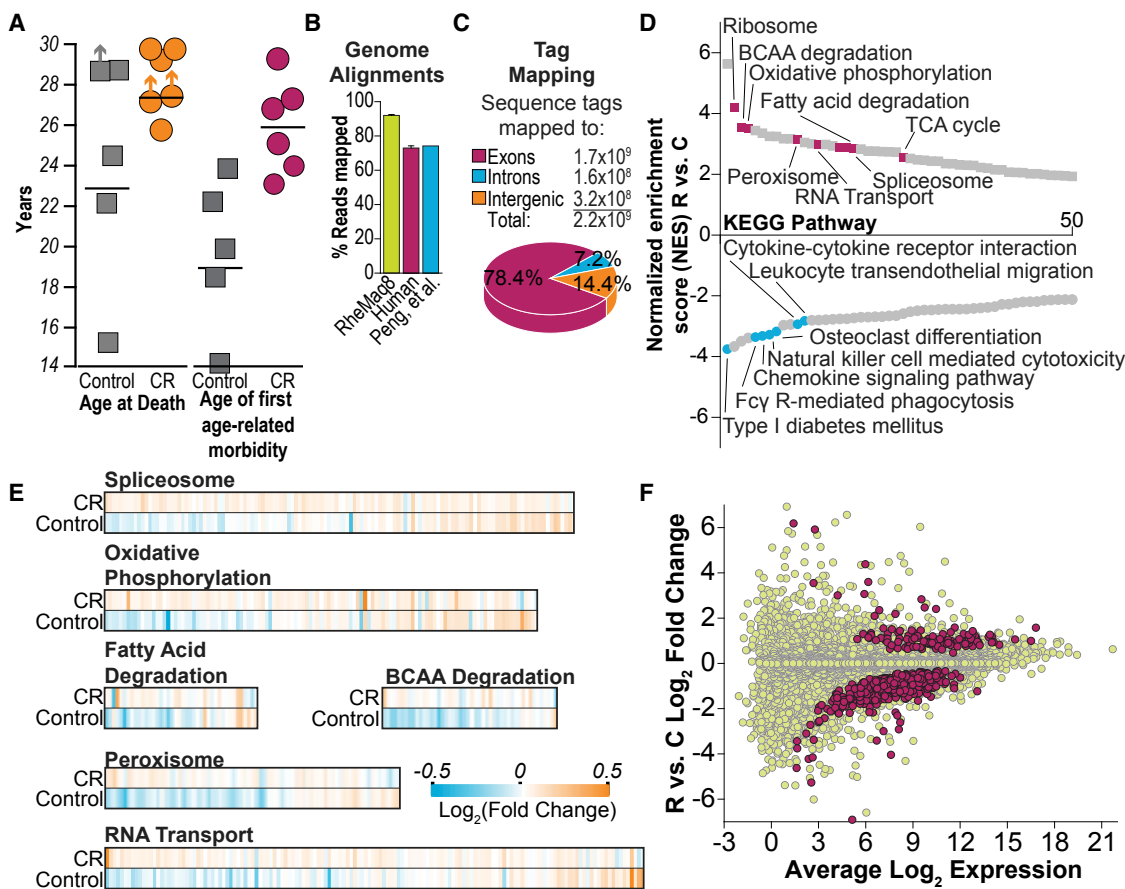


Figure 1. Transcriptional Response to CR Is Enriched for Metabolic Pathways

(A) Age at death and age of first age-related morbidity for the control and CR animals in this study. Upward arrows indicate animals that are still alive. See also Figure S1.

(B) Comparison of the percentage of reads aligning to RheMac8 genome build, human genome GRCh38.p7, rhesus transcriptome.

(C) Percentage of sequence tags that mapped to various structure types of the genome.

(D) Pathway enrichment via GSEA, ranked according to normalized enrichment score. See also Table S1.

(E) Heatmap displaying the average 2-year transition of each diet group for all individual gene members of spliceosome, oxidative phosphorylation, fatty acid degradation, BCAA degradation, peroxisome, and RNA transport pathways.

(F) MA plot showing the full range of average log₂ fold change versus average expression for all transcripts (pale yellow); a crt function filter of 0.7 identified significantly differentially expressed transcripts highlighted in maroon (514). See also Table S2.

metabolite analysis, proteomics, and lipidomics, were analyzed longitudinally for each individual monkey to identify changes in steady-state levels of biological molecules from control and CR groups. Higher-order analysis was conducted across complete and unfiltered datasets to uncover pathways and processes that potentially contribute mechanistically to delayed aging by CR.

RESULTS

CR Regulates Hepatic Metabolism and RNA Processing at the Transcript Level

Liver biopsies were taken from 11 adult males (control, n = 5; CR, n = 6; 9 ± 3 years of age) from the University of Wisconsin Rhesus Monkey Caloric Restriction and Aging study (Colman et al., 2009) at baseline and again 2 years into the study. For the monkeys in this cohort the average age of death was

22.7 years for controls and 27.4 years for CR monkeys (Figure 1A): six monkeys died of age-related causes (three control and three CR), three are still alive at the time of this report (one control and two CR), and two died of non-age-related conditions (one control and one CR). The first incidence of age-related disease or disorder occurred significantly earlier for controls at 19.0 years compared with 25.9 years for CR monkeys ($p < 0.05$). Biometric data and fasting plasma specimens were collected at both time points and linear mixed models were used to evaluate differences between controls and CR in the transition from 0 to 2 years. Bodyweight, lean mass, fat mass, and percentage adiposity were lower with CR (Figure S1A). Plasma levels of triglycerides and cholesterol were not different between groups at either time point (Figure S1B). Levels of glucose and insulin were lower in CR animals and insulin sensitivity was improved, with significant diet by time interactions detected for all parameters.

To generate an unbiased view of the liver transcriptional response to CR, we conducted RNA sequencing (RNA-seq) analysis ($n = 5$ per diet, per year), resulting in 864 million sequencing reads. After trimming, reads were aligned to the most recent version of the rhesus macaque genome, RheMac8, with approximately 92% of reads mapping uniquely. Approximately 70% of reads from the rhesus monkey transcriptome mapped to the human genome (GRCh38.p7), matching previous reports (Peng et al., 2015) (Figure 1B). Among the total of 2.2 billion sequence tags, 78% mapped to exons, 7% to introns, and 14% to intergenic regions (Figure 1C). Approximately 22,000 transcripts from 18,000 genes were detected, identified, and quantified. To assess functional enrichment, we conducted Kyoto Encyclopedia of Genes and Genomes (KEGG) pathway analysis using gene set enrichment analysis (GSEA) (Subramanian et al., 2005). The 2-year transition for each transcript for each animal in each group was calculated and the difference between groups for each transcript was used as the input. Following multiple testing adjustment (Benjamini-Hochberg with false discovery rate [FDR] <0.05), pathways were rank ordered based on enrichment value (Figure 1D; Table S1). Downregulated pathways largely included immune and inflammation pathways, while upregulated pathways included the ribosome, branched-chain amino acid (BCAA) degradation, oxidative phosphorylation, peroxisome, fatty acid degradation, RNA transport, and the spliceosome (Figure 1E). Several of these pathways constitute the tissue-type independent transcriptional signature of CR identified previously in mice (Barger et al., 2015).

The enrichment of the spliceosome was unexpected; a link between CR and RNA processing was unknown until recently when splicing was identified as a component of the CR response in *Caenorhabditis elegans* (Heintz et al., 2016). Based on RNA-seq data, the response to CR in primates included many components of the splicing process: dead-box RNA helicases that alter mRNA structure and participate in spliceosome assembly (*DDX23, 39B, 42, 46, and 5*), heterogeneous nuclear ribonucleoproteins that influence pre-mRNA processing (*HNRNPC, PK, PM, and PU*), LSM proteins that mediate U4/U6 small nuclear ribonucleoprotein particle (snRNP) formation (*LSM2-7*), spliceosome complex constituent proteins (*PRPF18, 19, 3, 31, 38A, 38B, 4, 40A, 6, and 8, RBM17, 22, 25, and 8A, SF3A1, A2, and A3, SF3B1, 14, 2–5*), and regulatory factors that influence the splicing of specific targets (*TRA2A and B, PUF60, NCBP1 and 2*). These data indicate that multiple aspects of RNA processing are differentially regulated in response to CR.

Monkeys are genetically heterogeneous and even with the longitudinal component in these analyses there was considerable variability among a subset of the transcripts identified that confounds detection of significantly changing genes. To identify individual genes responding to CR we filtered out highly variable transcripts by calculating the critical coefficient (crt) and applying a 0.7 crt threshold (Moskvin et al., 2015). Analysis of median-normalized 2-year transitions for the filtered genes yielded 514 transcripts as significantly different between control and CR animals (Figure 1F; Table S2). Pathways significantly enriched with CR were largely related to inflammation and immune function. Metabolism-related pathways, including fructose and mannose metabolism, carbon metabolism, regulation of lipolysis, pyruvate metabolism, and purine metabolism pathways,

were identified but did not survive the p value correction, likely due to low enrichment scores.

CR Directs Alternate Transcript Usage

The enrichment of the spliceosome and RNA transport pathways raised the possibility that CR might engage an alternate means of gene expression regulation through changes in exon usage. We found 2,205 of the 18,288 genes in the transcriptome yielded multiple transcripts (Figure 2A). Among the 514 CR-responsive genes described above, 70 (14%) had more than one isoform (Figure 2B), including metabolism-related genes such as *PEX11B, APOL4, and LSR*, associated with regulation of lipid metabolism. We next investigated whether changes in exon usage might occur in response to CR independent of differences in total transcript levels. DEXseq exon counting analysis identified 189,697 exons, of which 13,161 exons representing 4,496 genes were significantly different between the 0- and 2-year time points for CR animals (unadjusted $p < 0.05$). Enrichment analysis revealed 43 significantly enriched pathways representing multiple metabolic and RNA processing pathways (Figure 2C; Table S3). Multiple testing correction was applied to investigate individual exons responding to CR; 455 instances in 387 genes were found to have significant differences in the usage of specific exons (Figure 2D; Table S3). This contrasts with only nine cases of exon changes in six genes identified for controls, a 64-fold enrichment in exon switching with CR. PCR using primers to amplify across exon junctions confirmed the presence of transcripts with differences in exon usage (Figures 2E and S2). Sample exon maps of *MGLL*, a lipid-metabolism-related gene, and *PLRG1*, a spliceosome component, show usage changes in multiple exons with CR (Figure 2F). Sashimi plots (Figure 2G) showing sequencing reads mapped against the reference genome reveal different types of exon usage changes, with examples including exon skipping (*LSR*) and alternate exon inclusion (*FGFR2*). Notably, less than 6% of the genes regulated at the level of exon switching by CR were also identified as differentially expressed at the total transcript level, suggesting that this is an entirely separate means of gene expression regulation recruited by CR.

CR Impinges on Lipid and RNA Processing at the Protein Level

Protein abundance does not always correlate with transcript abundance, in particular under conditions of adaptive change (Grun et al., 2014). To determine whether factors regulated at the protein level overlapped with those identified by transcriptional analysis and whether other aspects of the primate CR response might be uncovered, we investigated the impact of CR on the hepatic proteome. Liquid chromatography-tandem mass spectrometry (LC-MS/MS) analysis identified and quantified 3,243 proteins ($n = 4$ per diet, per year) (Figure 3A). Over half of the mitochondrial proteome (606 proteins) was captured (Figure 3B), based on the MitoCarta (Calvo et al., 2016). Examination of 2-year fold changes revealed differences in the transitions of 274 proteins between control and CR animals (unadjusted $p < 0.05$) (Figure 3A; Table S5), with mitochondrial proteins representing 18%. Pathway analysis including all responsive proteins independent of directionality identified four

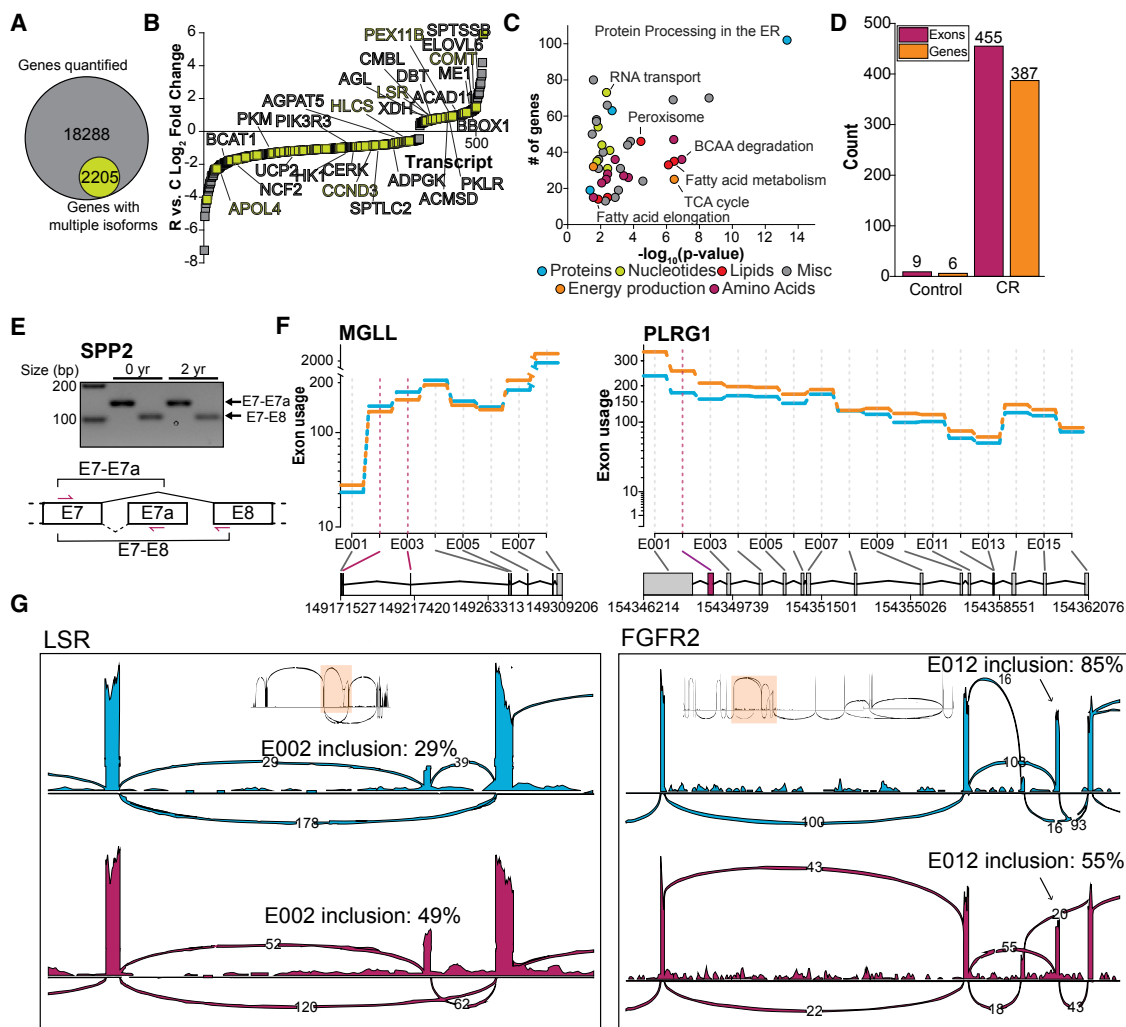


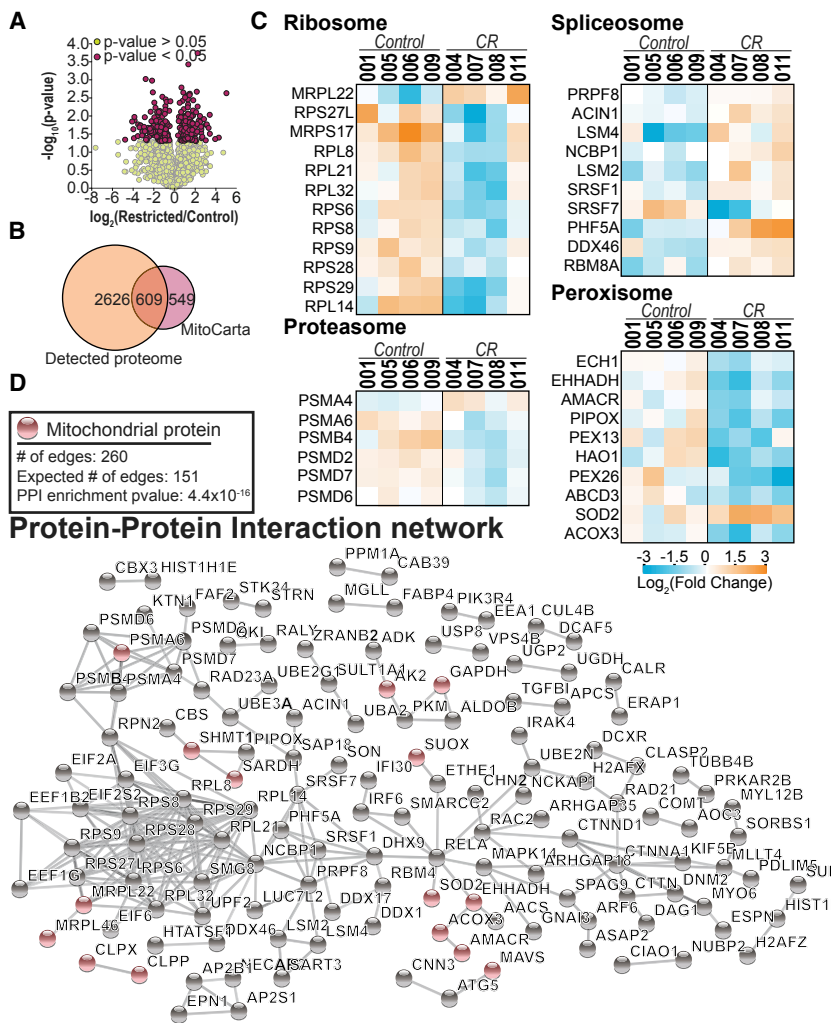
Figure 2. Altered RNA Processing Is a Feature of the Response to CR

- (A) Venn diagram displaying the genes quantified and the genes present as more than one transcript isoform.
- (B) Rank order plot of CR regulated genes. Those with more than one isoform are in green (70).
- (C) Pathway analysis of genes with exon usage changes during the 0 to 2-year transition, proteins (blue), nucleotides (green), lipids (red), energy production (orange), and amino acids (purple); adjusted p < 0.05. See also Table S3.
- (D) Comparison of the number of exon changes and corresponding genes in control and CR animals.
- (E) Agarose gels of PCR products generated using primers to specific usage of exons, as validation of the exon usage changes resulting from DEXseq analysis. See also Figure S2.
- (F) Example exon map for MGLL (left) and PLRG1 (right).
- (G) Sashimi plots for LSR (left) and FGFR2 (right), displaying the sequencing read mappings at the 0-year (blue, top) and 2-year (purple, bottom) time points.

that passed Benjamini-Hochberg correction, including peroxisomal, proteasomal, ribosomal, and spliceosome pathways (Figure 3C).

A difference in protein translation and turnover with CR is suggested in the identification of proteasomal and ribosomal pathways that were both downregulated. The proteasomal proteins included members of the α and β ring structures of the 20S (PSMA4, PSMA6, PSMB4), and non-ATPase components of the 19S regulator (PSMD2, PSMD6, PSMD7). The ribosomal pathway included ten ribosomal and two mitochondrial ribosomal proteins each from both the small and large subunits, consistent with the prevailing view that CR is associated

with growth inhibition. Although the transcriptional data indicated these pathways were increased with CR, we note that the molecular profiling presented reflects steady state and cannot inform about flux or turnover. Changes in lipid processing are suggested in the enrichment of the peroxisomal pathway among the significantly changing proteins. Proteins in the peroxisomal pathway included enzymes involved in β (ECH1, EHHADH) and α oxidation (HAO1), reactive oxygen species scavenging (SOD2), and membrane-associated peroxisomal biogenesis factors (PEX13, PEX26), with a mix of increased and decreased abundance among proteins of the pathway. The directionality of response to CR on the



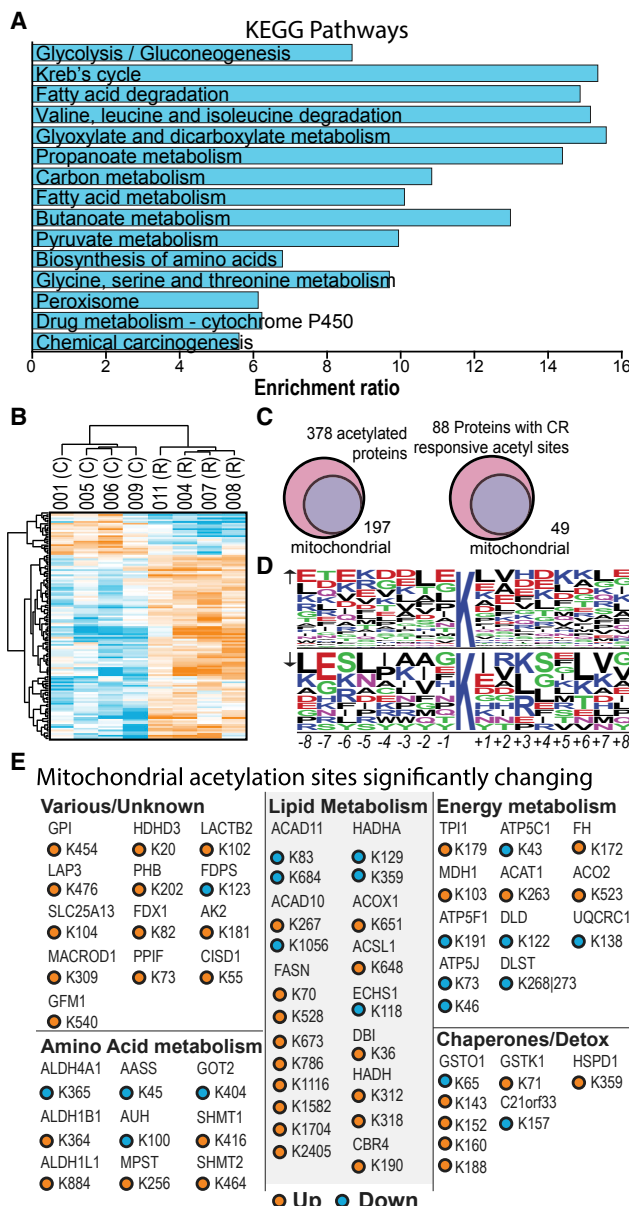
spliceosome was consistent with the transcriptional data, where CR predominantly increased abundance of component proteins. The spliceosome pathway included pre-mRNA splicing factors (LSM2, LSM4, SRSF1, SRSF7, NCBP1), spliceosome complex members (PHF5A, PRPF8), and associated regulators (ACIN1, RBMS8A, DDX46). Taking a broader view, we next investigated links among pathways enriched by CR. String analysis of the CR-enriched proteome revealed a higher than expected level of interconnectedness among proteins (Szklarczyk et al., 2015) (Figure 3D), with significantly more edges than expected by random chance (260 versus 151, p value = 4.4×10^{-16}), and pointing to the possibility that the response to CR is coordinated among pathways. Differences between transcript and protein data led us to investigate how well the CR-responsive proteome was represented in the transcriptional data. We found congruence in direction of effect for 48% of proteins responsive to CR, but less than 1% of the significantly changing transcripts (crt filtered to 0.7) informed of significant differences at the corresponding protein levels. This lack of congruence is not entirely unexpected, as similar effects have been observed in other large-scale transcript/protein comparisons (Grun et al., 2014; Kamkina et al., 2016; Maier et al., 2009).

Figure 3. Proteomic Response to CR Is Enriched for Peroxisomes, Protein and RNA Processing

(A) Volcano plot displaying proteins quantified. Statistically significant proteins (274) are highlighted in maroon. See also Table S4.
 (B) Venn diagram showing the overlap between the experimentally detected proteome and proteins identified in MitoCarta.
 (C) Heat maps of longitudinal log₂ fold change for KEGG pathways (adjusted $p < 0.05$) enriched in the proteome: ribosome, spliceosome, proteasome, and peroxisome.
 (D) Network identified by String. Proteins with no interactions are hidden; proteins identified as mitochondrial according to MitoCarta are highlighted in orange.

CR Affects the Mitochondrial Acetylome

Transcriptional evidence for CR-induced changes to metabolism prompted an investigation of acetylation, a post-translational modification linked to cellular metabolism and the availability of acetyl coenzyme A (CoA) (Choudhary et al., 2014). Longevity-enhancing diets such as CR (Hebert et al., 2013) and the ketogenic diet (Roberts et al., 2017) are reported to increase levels of acetylation in liver in mice. Lysine ε-acetylation is a major feature in the regulation of mitochondrial metabolism and 63% of proteins localized to mitochondria contain lysine acetylation sites (Baeza et al., 2016). LC-MS/MS of the immuno-enriched acetylproteome detected 946 acetylated peptides that aligned to 378 unique proteins. The monkey acetylome represented several metabolic pathways (Figure 4A), including the Krebs cycle, fatty acid degradation, glycolysis/gluconeogenesis, and synthesis and degradation of ketone bodies, similar to what has been previously described in rodents (Hallows et al., 2011; Hebert et al., 2013). CR induced changes in 128 acetyl proteoforms aligning to 88 unique proteins (unadjusted $p < 0.05$). Hierarchical clustering of the longitudinal change in abundance of proteoforms revealed the majority of CR-responsive marks to be upregulated (Figure 4B, Table S5). Proteins responsive to CR at the level of acetylation included endoplasmic reticulum (ER)-associated TERC and SLC27A2, peroxisomal EHHADH and ACSL1, and cytosolic PGM1, UGP2, PYGL, and GAPDH. Consistent with published rodent data, about half of all proteins detected with acetylation marks were mitochondrial, and 40 of the 88 CR-responsive acetyl proteoforms were mitochondrial (Figure 4C). The peptide sequences surrounding significantly changing mitochondrial acetylation sites were examined to investigate sequence motifs (Figure 4D). Upregulated marks displayed a preference for acidic residues N-terminal to the acetyl site, and a preference for basic amino acids C-terminal to the acetyl site was identified for downregulated marks.

**Figure 4. CR Induces Mitochondrial Acetylome Remodeling**

(A) Top 15 KEGG pathways enriched in the acetylated proteins.

(B) Acetyl isoforms (128) with significantly different 2-year transitions between control and CR ($p < 0.05$). Hierarchical clustering (cosine, furthest neighbor) separated acetyl isoforms into two large groups, segregating by diet. See also Table S5.

(C) Left: Venn diagrams of total proteins with acetylation marks (378) including MitoCarta designation as mitochondrial (197). Right: proteins with significantly changing acetyl isoforms (88) including mitochondrial proteins (40).

(D) Motif analysis of CR-responsive mitochondrial acetyl sites.

(E) Significantly different acetyl sites on mitochondrial proteins (upregulated, orange; downregulated, blue).

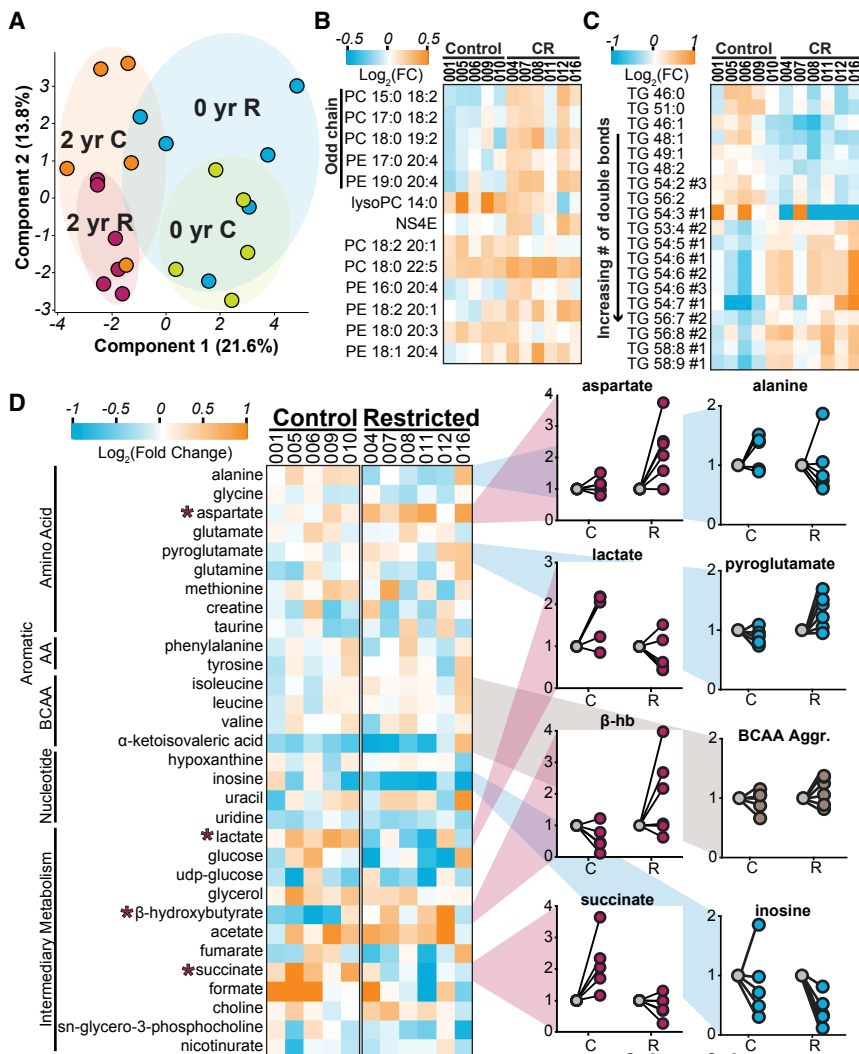
Mitochondrial CR-responsive proteins included enzymes in amino acid metabolism, the electron transport chain, lipid metabolism, and the TCA cycle (Figure 4E). Finally, DDX39b and DHX9 associated with RNA processing were also differentially

acetylated with CR. These data show that acetylation changes induced by CR fall into the same pathways that were identified as CR responsive in the transcriptome and proteome datasets.

CR Induces Changes in Hepatic Metabolite Profiles

Lipid metabolism pathways were identified in the transcriptional, proteomic, and acetylomic responses to CR. To seek independent confirmation that CR affects lipid metabolism we conducted LC-MS/MS analysis of hepatic nonpolar metabolites ($n = 5-6$ per diet, per year). Library standards, followed by manual spectral validation, were used to quantify 246 hepatic lipids, including glycerolipids, phosphoglycerolipids (PLs), and free fatty acids (Table S6). Principal component analysis separated the data first primarily by time (0 versus 2 years), while the second principal component largely separated the data by diet (Figure 5A), and together explained 36% of the variability in hepatic lipid composition. Changes in lipid composition over the 2-year transition identified 32 unique lipid species significantly different between the two groups (unadjusted $p < 0.05$) and included PL, ceramide (Figure 5B), and triacylglycerols (TGs) (Figure 5C). PL became more abundant for CR animals, and 5 of the 12 PL species were odd-chain fatty acids. Saturated TG species increased in control monkeys over the 2-year transition but were lower with CR, while unsaturated TG species became less abundant in controls and more abundant in CR. The biological significance of these changes in TG composition is currently unclear but likely extends to the composition of hepatic exported lipoproteins.

Nuclear magnetic resonance (NMR) spectroscopy was used to characterize the effect of CR on soluble liver metabolites. Characteristic proton chemical shifts from one-dimensional NMR spectra identified specific metabolites, while two-dimensional total correlation spectroscopy (TOCSY) and ^1H - ^{13}C heteronuclear single quantum coherence spectroscopy (HSQC) analyses yielded cross-correlation peaks that confirmed metabolite identification. In sum, 31 metabolites were quantified, including amino acids, BCAAs, aromatic amino acids, nucleotides, and molecules involved in intermediary metabolism. Longitudinal differences between control and CR were detected for four metabolites (unadjusted $p < 0.05$) (Figure 5D), including increased aspartate and β -hydroxybutyrate (β -hb), and decreased lactate and succinate. Previous studies have reported changes in hepatic enzymes in mice on CR, including increased gluconeogenic activity (Hagopian et al., 2003a), increased succinate dehydrogenase, increased acyl-CoA dehydrogenase, increased β -hb dehydrogenase, and decreased lactate dehydrogenase (Hagopian et al., 2013). These changes in metabolites suggest increased utilization of ketone body metabolism, a known feature of CR, and increased anaplerotic pathways. Lower lactate levels could reflect differences in use or uptake in the CR liver. Although both transcriptome and proteome analyses point to differences in BCAA pathways as an outcome of CR, differences in steady-state levels of any of the BCAAs were not detected. Both aspartate and lactate showed significant correlations with biometric and serum measures, although the relationships were not equivalent between diet groups (Figure S3). These data suggest that CR monkeys differ in extent of engagement of anaplerotic and glucose-sparing pathways.



CR Induces a Highly Integrated Reprogramming of Hepatic Metabolism

Although the identification of RNA processing as part of the CR response is new, the presence of recurring themes of metabolism and protein synthesis are along the lines of what might be expected based on rodent data, and were consistent across each of the molecular profiling platforms. This led us to question if CR-directed regulation of these distinct cellular processes might be coordinated, and if the regulatory mechanisms engaged in the CR response might be interlinked. The longitudinal design and the fact that all data were generated from the same tissues facilitated a higher-order analysis. A large correlation matrix was constructed using data generated by each of the above platforms from eight animals at time zero ($\sim 20,000$ molecules) to establish a baseline. Pearson correlation coefficients were calculated for the $\sim 4 \times 10^8$ pairwise comparisons and rendered by hierarchical clustering. Using a cut-off coefficient of magnitude 0.8 or greater, over 2,700 clusters were identified with average cluster occupancy of 7–8 molecules (Figure S4A), suggesting coordination among hepatic metabolites, transcripts, and proteins is accomplished through an extensive

Figure 5. CR-Induced Changes in Hepatic Lipids and Soluble Metabolites

(A) Principal component analysis of the lipid species detected for each diet group and time point. The first two components explain approximately 40% of the variance. See also Table S6.

(B) Heatmap of the glycerophospholipids with significant differences in 2-year trajectories. NS4E, N-(hexadecanoyl)-sphing-4-enine.

(C) Heatmap of the triacylglycerolipids with significant differences in 2-year trajectories ordered by the degree of saturation. # designations provide a unique identifier for species that were isobaric.

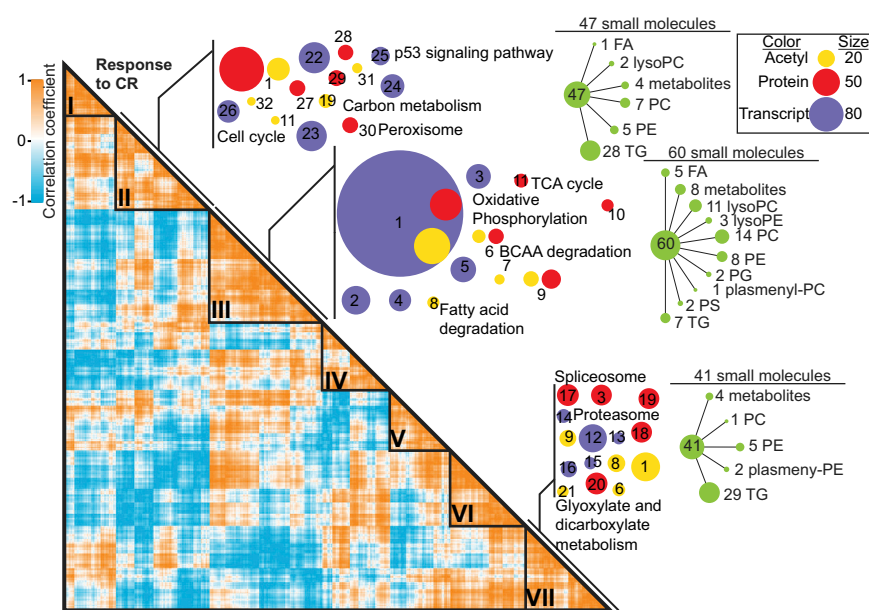
(D) Heatmap showing the 2-year trajectories of 31 metabolites quantified by NMR. Right, flyout graphs with 0-year samples set to 1. See also Figures S2 and S3.

network of small regulatory nodes. The same strategy was then used to interrogate the impact of the 2-year transition on the relationships among molecules as a function of diet. For CR animals ($n = 4$ per time point), hierarchical clustering of correlations revealed 90 clusters with average cluster occupancy of >220 molecules that organized into seven mega-clusters (Figure 6). These mega-clusters included multiple aspects of metabolism interlinked with growth and RNA processing pathways, confirming the importance of themes identified in each of the individual platform analysis (Table S7), and suggesting that the response to CR is highly coordinated. Constraining the hierarchy to that established for the CR transition yielded no clusters for pairwise comparisons for controls, indicating that

the manner in which processes are integrated in CR animals is entirely different from that of controls (Figure S4B). These data demonstrate that the inter-relationship among hepatic factors and pathways in CR animals is distinct from that of controls and that the response to diet is highly coordinated, and provide independent corroborating evidence that the themes identified by earlier analysis are prominent features of the CR response.

CR Predictive Model Network Genes Are Processed at the RNA Level

We next conducted random forest predictive modeling to identify groups of molecules that might define the signature of CR. This machine learning approach interrogates a complete and unfiltered dataset using an iterative, unbiased process of hierarchical sorting to build decision trees from randomly selected molecules. For each iteration the effectiveness of the decision tree is evaluated and growth is trained for increasing accuracy: the ability to distinguish control from CR data. Random forest analysis was applied to each of the transcript, protein, and acetyl datasets over 8,000 iterations. Small molecule data were excluded due to insufficient size for effective tree construction.



cytokine-cytokine receptor interaction; 24, natural killer cell-mediated cytotoxicity; 25, p53 signaling pathway; 26, cell cycle; 27, metabolism of xenobiotics by cytochrome P450; 28, retinol metabolism; 29, chemical carcinogenesis; 30, peroxisome; 31, biosynthesis of amino acids; 32, glycine, serine, and threonine metabolism. Green balls indicate the number of small molecules identified in the highlighted clusters, broken down by molecule type. See also Table S7 and Figure S4.

Variables contributing to the cumulative models were ranked according to their importance in the model based on accuracy (weighted contribution), or Gini impurity index (variable importance) (Figure 7A). The acetylome model was highly enriched for enzymes of intermediary metabolism, including enzymes related to lipid metabolism, glycogen and glucose metabolism, and the TCA cycle. The proteome model was populated by metabolic enzymes, including those involved in lipid metabolism, peroxisomes, BCAA metabolism, and one carbon metabolism, and regulatory factors involved in intracellular trafficking, peroxisomes, regulation of RNA processing, and regulation of translation. The top protein was QKI, a protein involved in pre-mRNA splicing and mRNA nuclear export. The transcriptome model included multiple regulatory factors involved in cell structure, RNA processing, and chromatin remodeling or binding factors (Figure S5). Interestingly, the genes contributing to this model are different from those emerging from the prior analysis, perhaps because standard data mining views each data point individually, as opposed to machine learning where a cumulative model is generated.

To investigate connections within the random forest models we next applied String analysis. Variables from each model were limited to those with mean decrease in accuracy-associated $p < 0.05$. The acetylome model (97 marks, 72 unique proteins) contained a high degree of integration among variables, with twice the number of edges than would be randomly predicted (Figure S6A). String analysis of the proteome model (167 variables) identified the same number of edges as would be predicted by random chance (Figure S6B), and for the gene model (177 variables) substantially fewer edges than would be predicted by random chance were identified, with the exception of one highly connected node related to RNA processing (Fig-

Figure 6. Integrative Correlation Analysis Reveals the Metabolic Program of CR

Pearson correlation matrix of the changes in ~18,000 molecules over a 2-year transition for CR monkeys ($n = 4$). Hierarchical clustering of regression data (4×10^8 pairwise comparisons) revealed seven mega-clusters. Pathway analysis within clusters shown including contributions from transcriptome (blue), proteome (red), and acetylome (yellow), scaled as indicated. 1, Metabolic pathways; 2, Huntington's disease; 3, oxidative phosphorylation; 4, pyrimidine metabolism; 5, ribosome; 6, BCAA degradation; 7, seleno-compound metabolism; 8, fatty acid degradation; 9, carbon metabolism; 10, propanoate metabolism; 11, tricarboxylic acid (TCA) cycle; 12, protein processing in the ER; 13, protein export; 14, proteasome; 15, SNARE (soluble N-ethylmaleimide-sensitive factor attachment protein receptor) interactions in vesicular transport; 16, neurotrophin signaling pathway; 17, spliceosome; 18, Parkinson's disease; 19, non-alcoholic fatty liver disease; 20, Alzheimer's disease; 21, glyoxylate and dicarboxylate metabolism; 22, human T Cell lymphotropic virus 1 (HTLV-I) infection; 23,

ure S6C). We next asked whether aggregate data from all predictive models might yield a different perspective. Variables were combined from the three random forest models and trimmed for redundancy and uncharacterized genes. String analysis of this list revealed an extensively connected network (Figure 7B) with twice the number of edges detected than would be predicted by random chance. The CR network included nodes representing fatty acid metabolism, BCAA metabolism, carbon metabolism, and detoxification processes. We next asked if factors regulated at the level of RNA processing in response to CR featured in the network. Of the 403 genes that constitute the random forest network, 212 were identified as having differences in exon usage in response to CR (Table S8). These data suggest that CR establishes a highly integrated network that extends across multiple aspects of metabolism, and that regulation at the level of RNA is a major factor in the implementation of the CR program.

DISCUSSION

The NHP CR core network identified here includes several features that are consistent with what is known from CR studies in rodents. These include xenobiotic pathways, changes in amino acid metabolism and gluconeogenic pathways (Hagopian et al., 2003a), fatty acid metabolic pathways that align with the increased reliance on oxidative metabolism identified in rodents on CR (Bruss et al., 2010), mitochondrial energy and glucose metabolism pathways, and one carbon metabolism that has previously been linked to genetic models of longevity (Armstrong et al., 2014) and CR (Wang et al., 2017). BCAA metabolism has been linked to homeostatic metabolic regulation (Bifari and Nisoli, 2017); however, a role in the context of CR is relatively

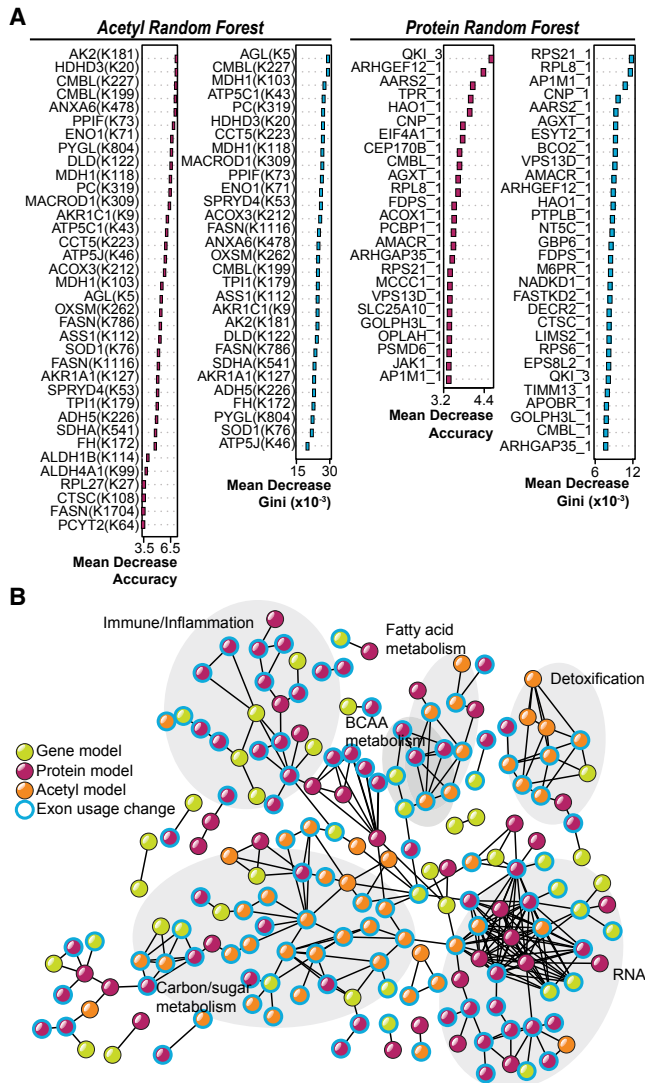


Figure 7. Random Forest Predictive Modeling Reveals CR Network Genes Regulated by RNA Processing

(A) Top molecules from random forest classifiers generated separately for acetylome and proteome data, ranked by mean decrease accuracy and Gini index. See also Figure S5.

(B) Network identified by String using the random forest predictive model from acetylome (orange), proteome (magenta), and transcriptome (green) data. Proteins with no interactions are hidden. The network contained 308 interactions, significantly more than expected from the size of the input (224 edges expected by chance; p value 5.6×10^{-8}). Genes displaying a significant CR-induced switch in exon usage are highlighted (blue). See also Table S8 and Figure S6.

new. The increase in hepatic β -hb also matches rodent studies (Hagopian et al., 2003b) and may be important given the link between ketone bodies and metabolic health (Newman and Verdin, 2014). We also identified several new features of CR: first, the engagement of RNA processing mechanisms involved in diverse cellular processes; second, the recruitment of parallel mechanisms of gene expression regulation at the transcriptional, post-transcriptional, and post-translational levels; third, a highly integrated program that spans multiple aspects of metabolism

and growth regulation; fourth, the distinct lipid and metabolite profiles suggesting that liver metabolism differs substantially between control and CR monkeys; and, fifth, the recurring theme of lipid metabolism and peroxisomal function, suggesting a key role for lipid metabolic integrity in health and aging.

The potential role of RNA processing in implementing the CR program is of particular interest. Roles for splicing events in murine and stem cell aging have recently emerged (Crews et al., 2016; Rodriguez et al., 2016), and a link to RNA processing has also been identified in genome-wide association studies of human longevity (Lee et al., 2016). A prior study of the murine hepatic response to CR identified three splicing-associated genes (Swindell, 2009) and a recent study of *C. elegans* aging also identified a role for RNA processing events in aging and in dietary restriction (Heintz et al., 2016). Importantly, data presented here identified spliceosome and RNA processing factors in the transcriptome, proteome, and acetylome analysis, and exon analysis identified a clear recruitment of RNA processing mechanisms such as exon skipping and alternate exon usage specifically in CR tissue. Higher-level analysis of multi-platform data identified a predictive model network where over 50% of constituent genes were identified in the independent exon-level analysis as being subject to post-transcriptional regulation directly as a result of CR. We recently identified CR-induced changes in the abundance of circulating microRNAs (miRNAs) in an older group of rhesus monkeys from the CR and aging cohort study, further supporting a role for RNA-based mechanisms in the CR response (Schneider et al., 2017). Pathways of metabolism, growth regulation, and the spliceosome were among the putative targets of CR-responsive serum miRNA. The targets of CR-responsive miRNA represented 18% of the RNA-linked pathways identified as CR responsive in this study, at both the transcriptome (71 of 391 factors) and proteome levels (15 of 83 factors).

The next important steps will be to discover whether CR also impinges on RNA processing in other tissues in NHPs and to discover how and why these changes are induced. Mechanistic studies to establish the identity of factors regulating RNA processing in response to CR, how specificity in exon switching is accomplished, and to define the functional consequence of the resulting transcript isoforms might best be conducted using murine models that are better suited than monkeys for genetic approaches. Given the extraordinary translatability of the rhesus model, mechanisms of CR including RNA processing are highly likely to be important in human aging and strategies to delay age-associated disease.

Limitations of Study

The purpose of these investigations was to elucidate the hepatic molecular networks responsive to CR in the highly translatable rhesus macaque. As always, there are trade-offs in conducting studies using a long-lived genetically heterogeneous model that is so closely related to humans. First, the numbers of animals in the cohort are limited due to the cost of housing and clinical care, factors that are exacerbated by the longevity of the rhesus model, which has a median lifespan in captivity of 26 years. Second, the heterogeneity among individual animals is similar to that of humans and although the use of dual time points for each monkey alleviates some of the difficulties, the

innate variability in measures among the cohort remains a challenge. A third consideration is the availability of tissues from animals of this cohort. Biopsies were only taken on two occasions during the 28-year-long CR and aging study and then only for a subset of monkeys. The limited amounts of available tissue have precluded follow-up mechanistic studies guided by the insights afforded here that might otherwise be applied using a candidate approach. Fourth, the strength of the rhesus model is translatability; ordinarily, rhesus studies are focused on confirmation of conservation of mechanisms and it is unusual to identify mechanisms of delayed mammalian aging first in a primate model as we do here. Although further in-depth investigation may yet be conducted among other tissues from the monkeys in this study, it is almost certain that the mechanistic studies required to follow up on these new leads will require jumping species. A fifth issue is the use of unbiased molecular profiling techniques that create considerable statistical challenges due to correction for multiple testing. Here we report the statistical approach undertaken for each element of the study and the rationale for each of the tests and strategies employed. We have tried to offset some of the complications of large-scale profiling by using the same hepatic tissues to generate data on each platform. A final caveat for this study that we fully acknowledge is the somewhat descriptive nature of the findings. Large-scale interrogation techniques and integrative analyses were employed to create a high-level view of the CR response; this revealed the involvement of many pathways canonically linked to CR, including metabolism, xenobiotics, and inflammation. The inclusion of RNA processing mechanisms both within individual datasets and across the entire CR-responsive network is highly suggestive of a role for RNA processing in the implementation of the CR program; however, these studies do not demonstrate causality. Specifically, the extent of the role played by RNA processing in implementing the CR response cannot be inferred from this study, nor can the requirement for such mechanisms for the eventual longevity benefits observed with CR be assigned. As such, this work should not be used to infer the primacy of any features described as CR responsive, but instead represents a comprehensive, integrated account of the molecules and pathways recruited by CR that may underlie the longevity benefits.

STAR★METHODS

Detailed methods are provided in the online version of this paper and include the following:

- KEY RESOURCES TABLE
- CONTACT FOR REAGENT AND RESOURCE SHARING
- EXPERIMENTAL MODEL AND SUBJECT DETAILS
- METHOD DETAILS
 - Metabolomics
 - Lipidomics
 - Proteomics and Acetyl-Proteomics
 - Transcriptomics
 - Data Analysis
 - Data Integration
- QUANTIFICATION AND STATISTICAL ANALYSIS
- DATA AND SOFTWARE AVAILABILITY

SUPPLEMENTAL INFORMATION

Supplemental Information includes six figures and eight tables and can be found with this article online at <https://doi.org/10.1016/j.cmet.2018.01.014>.

ACKNOWLEDGMENTS

This work was supported by NIH grants AG047358 (R.M.A./R.J.C.), AG040178 (R.M.A./R.J.C.), GM108538 and GM118110 (J.J.C.), and by the Glenn Foundation for Medical Research (R.M.A.). T.W.R. and V.B.C. were supported by LM007359 T32 fellowships, and J.P.C. was supported by AG000213 T32 fellowship. This study was made possible in part by NIH grant P41 GM103399 awarded to NMRFAM, NCRR/ORIP grants P51RR000167/P51OD011106 awarded to the WNPRC, and was conducted with the use of resources and facilities at the William S. Middleton Memorial Veterans Hospital Madison, WI. All data are available upon request.

AUTHOR CONTRIBUTIONS

T.W.R., M.S.B., V.B.C., J.P.C., P.D.H., M.J.P.R., J.L.S., and R.J.C. generated data. T.W.R., H.R.E., J.L.M., J.M.D., J.J.C., and D.M.P. conducted analysis and contributed to data interpretation. S.J.M., T.W.R., and I.M.O. conducted the dataset integration analysis. T.W.R., M.S.B., and R.M.A. wrote the manuscript.

DECLARATION OF INTERESTS

The authors declare no competing interests.

Received: May 23, 2017

Revised: September 29, 2017

Accepted: January 28, 2018

Published: March 6, 2018

REFERENCES

- Anders, S., Pyl, P.T., and Huber, W. (2015). HTSeq—a Python framework to work with high-throughput sequencing data. *Bioinformatics* 31, 166–169.
- Anders, S., Reyes, A., and Huber, W. (2012). Detecting differential usage of exons from RNA-seq data. *Genome Res.* 22, 2008–2017.
- Armstrong, V.L., Rakoczy, S., Rojanathammanee, L., and Brown-Borg, H.M. (2014). Expression of DNA methyltransferases is influenced by growth hormone in the long-living Ames dwarf mouse *in vivo* and *in vitro*. *J. Gerontol. A Biol. Sci. Med. Sci.* 69, 923–933.
- Baeza, J., Smallegan, M.J., and Denu, J.M. (2016). Mechanisms and dynamics of protein acetylation in mitochondria. *Trends Biochem. Sci.* 41, 231–244.
- Balasubramanian, P., Howell, P.R., and Anderson, R.M. (2017a). Aging and caloric restriction research: a biological perspective with translational potential. *EBioMedicine* 21, 37–44.
- Balasubramanian, P., Mattison, J.A., and Anderson, R.M. (2017b). Nutrition, metabolism, and targeting aging in nonhuman primates. *Ageing Res. Rev.* 39, 29–35.
- Barger, J.L., Anderson, R.M., Newton, M.A., da Silva, C., Vann, J.A., Pugh, T.D., Someya, S., Prolla, T.A., and Weindruch, R. (2015). A conserved transcriptional signature of delayed aging and reduced disease vulnerability is partially mediated by SIRT3. *PLoS One* 10, e0120738.
- Bates, D., Mächler, M., Bolker, B., and Walker, S. (2015). Fitting linear mixed-effects models using lme4. *J. Statist. Softw.* <https://doi.org/10.18637/jss.v067.i01>.
- Bifari, F., and Nisoli, E. (2017). Branched-chain amino acids differently modulate catabolic and anabolic states in mammals: a pharmacological point of view. *Br. J. Pharmacol.* 174, 1366–1377.
- Bingol, K., Li, D.W., Bruschweiler-Li, L., Cabrera, O.A., Megraw, T., Zhang, F., and Bruschweiler, R. (2015). Unified and isomer-specific NMR metabolomics database for the accurate analysis of (13)C-(1)H HSQC spectra. *ACS Chem. Biol.* 10, 452–459.

- Bruss, M.D., Khambatta, C.F., Ruby, M.A., Aggarwal, I., and Hellerstein, M.K. (2010). Calorie restriction increases fatty acid synthesis and whole body fat oxidation rates. *Am. J. Physiol. Endocrinol. Metab.* 298, E108–E116.
- Calvo, S.E., Clouser, K.R., and Mootha, V.K. (2016). MitoCarta2.0: an updated inventory of mammalian mitochondrial proteins. *Nucleic Acids Res.* 44, D1251–D1257.
- Choudhary, C., Weinert, B.T., Nishida, Y., Verdin, E., and Mann, M. (2014). The growing landscape of lysine acetylation links metabolism and cell signalling. *Nat. Rev. Mol. Cell Biol.* 15, 536–550.
- Clos, L.J., 2nd, Jofre, M.F., Ellinger, J.J., Westler, W.M., and Markley, J.L. (2013). NMRbot: Python scripts enable high-throughput data collection on current Bruker BioSpin NMR spectrometers. *Metabolomics* 9, 558–563.
- Colman, R.J., and Anderson, R.M. (2011). Nonhuman primate calorie restriction. *Antioxid. Redox Signal.* 14, 229–239.
- Colman, R.J., Anderson, R.M., Johnson, S.C., Kastman, E.K., Kosmatka, K.J., Beasley, T.M., Allison, D.B., Cruzen, C., Simmons, H.A., Kemnitz, J.W., et al. (2009). Caloric restriction delays disease onset and mortality in rhesus monkeys. *Science* 325, 201–204.
- Colman, R.J., Beasley, T.M., Kemnitz, J.W., Johnson, S.C., Weindruch, R., and Anderson, R.M. (2014). Caloric restriction reduces age-related and all-cause mortality in rhesus monkeys. *Nat. Commun.* 5, 3557.
- Cox, J., and Mann, M. (2012). 1D and 2D annotation enrichment: a statistical method integrating quantitative proteomics with complementary high-throughput data. *BMC Bioinformatics* 13 (Suppl 16), S12.
- Crews, L.A., Balaian, L., Delos Santos, N.P., Leu, H.S., Court, A.C., Lazzari, E., Sadarangani, A., Zipeto, M.A., La Clair, J.J., Villa, R., et al. (2016). RNA splicing modulation selectively impairs leukemia stem cell maintenance in secondary human AML. *Cell Stem Cell* 19, 599–612.
- de Magalhaes, J.P., Curado, J., and Church, G.M. (2009). Meta-analysis of age-related gene expression profiles identifies common signatures of aging. *Bioinformatics* 25, 875–881.
- Dobin, A., Davis, C.A., Schlesinger, F., Drenkow, J., Zaleski, C., Jha, S., Batut, P., Chaisson, M., and Gingeras, T.R. (2013). STAR: ultrafast universal RNA-seq aligner. *Bioinformatics* 29, 15–21.
- Durinck, S., Moreau, Y., Kasprzyk, A., Davis, S., De Moor, B., Brazma, A., and Huber, W. (2005). BioMart and Bioconductor: a powerful link between biological databases and microarray data analysis. *Bioinformatics* 21, 3439–3440.
- Fok, W.C., Bokov, A., Gelfond, J., Yu, Z., Zhang, Y., Doderer, M., Chen, Y., Javors, M., Wood, W.H., 3rd, Becker, K.G., et al. (2014). Combined treatment of rapamycin and dietary restriction has a larger effect on the transcriptome and metabolome of liver. *Aging Cell* 13, 311–319.
- Fontana, L., and Partridge, L. (2015). Promoting health and longevity through diet: from model organisms to humans. *Cell* 161, 106–118.
- Fox, J., and Weisberg, S. (2011). An R Companion to Applied Regression (Sage Publications).
- Geer, L.Y., Markey, S.P., Kowalak, J.A., Wagner, L., Xu, M., Maynard, D.M., Yang, X., Shi, W., and Bryant, S.H. (2004). Open mass spectrometry search algorithm. *J. Proteome Res.* 3, 958–964.
- Grun, D., Kirchner, M., Thierfelder, N., Stoeckius, M., Selbach, M., and Rajewsky, N. (2014). Conservation of mRNA and protein expression during development of *C. elegans*. *Cell Rep.* 6, 565–577.
- Hagopian, K., Ramsey, J.J., and Weindruch, R. (2003a). Caloric restriction increases gluconeogenic and transaminase enzyme activities in mouse liver. *Exp. Gerontol.* 38, 267–278.
- Hagopian, K., Ramsey, J.J., and Weindruch, R. (2003b). Influence of age and caloric restriction on liver glycolytic enzyme activities and metabolite concentrations in mice. *Exp. Gerontol.* 38, 253–266.
- Hagopian, K., Soo Hoo, R., Lopez-Dominguez, J.A., and Ramsey, J.J. (2013). Calorie restriction influences key metabolic enzyme activities and markers of oxidative damage in distinct mouse liver mitochondrial sub-populations. *Life Sci.* 93, 941–948.
- Hallows, W.C., Yu, W., Smith, B.C., Devries, M.K., Ellinger, J.J., Someya, S., Shortreed, M.R., Prolla, T., Markley, J.L., Smith, L.M., et al. (2011). Sirt3 promotes the urea cycle and fatty acid oxidation during dietary restriction. *Mol. Cell* 41, 139–149.
- Hebert, A.S., Dittenhafer-Reed, K.E., Yu, W., Bailey, D.J., Selen, E.S., Boersma, M.D., Carson, J.J., Tonelli, M., Balloon, A.J., Higbee, A.J., et al. (2013). Calorie restriction and SIRT3 trigger global reprogramming of the mitochondrial protein acetylome. *Mol. Cell* 49, 186–199.
- Heintz, C., Doktor, T.K., Lanjuin, A., Escoubas, C.C., Zhang, Y., Weir, H.J., Dutta, S., Silva-Garcia, C.G., Bruun, G.H., Morantte, I., et al. (2016). Splicing factor 1 modulates dietary restriction and TORC1 pathway longevity in *C. elegans*. *Nature* 541, 102–106.
- Jiang, H., Lei, R., Ding, S.W., and Zhu, S. (2014). Skewer: a fast and accurate adapter trimmer for next-generation sequencing paired-end reads. *BMC Bioinformatics* 15, 182.
- Jove, M., Naudi, A., Ramirez-Nunez, O., Portero-Otin, M., Selman, C., Withers, D.J., and Pamplona, R. (2014). Caloric restriction reveals a metabolomic and lipidomic signature in liver of male mice. *Aging Cell* 13, 828–837.
- Kamkina, P., Snoek, L.B., Grossmann, J., Volkers, R.J., Sterken, M.G., Daube, M., Roschitzki, B., Fortes, C., Schlappach, R., Roth, A., et al. (2016). Natural genetic variation differentially affects the proteome and transcriptome in *Caenorhabditis elegans*. *Mol. Cell Proteomics* 15, 1670–1680.
- Kanehisa, M., Furumichi, M., Tanabe, M., Sato, Y., and Morishima, K. (2017). KEGG: new perspectives on genomes, pathways, diseases and drugs. *Nucleic Acids Res.* 45, D353–d361.
- Kim, W., Bennett, E.J., Huttlin, E.L., Guo, A., Li, J., Possement, A., Sowa, M.E., Rad, R., Rush, J., Comb, M.J., et al. (2011). Systematic and quantitative assessment of the ubiquitin-modified proteome. *Mol. Cell* 44, 325–340.
- Kind, T., Liu, K.H., Lee, D.Y., DeFelice, B., Meissen, J.K., and Fiehn, O. (2013). LipidBlast in silico tandem mass spectrometry database for lipid identification. *Nat. Methods* 10, 755–758.
- Lee, B.P., Pilling, L.C., Emond, F., Flurkey, K., Harrison, D.E., Yuan, R., Peters, L.L., Kuchel, G.A., Ferrucci, L., Melzer, D., et al. (2016). Changes in the expression of splicing factor transcripts and variations in alternative splicing are associated with lifespan in mice and humans. *Aging Cell* 15, 903–913.
- Leng, N., Dawson, J.A., Thomson, J.A., Ruotti, V., Rissman, A.I., Smits, B.M., Haag, J.D., Gould, M.N., Stewart, R.M., and Kendziora, C. (2013). EBSeq: an empirical Bayes hierarchical model for inference in RNA-seq experiments. *Bioinformatics* 29, 1035–1043.
- Li, B., and Dewey, C.N. (2011). RSEM: accurate transcript quantification from RNA-Seq data with or without a reference genome. *BMC Bioinformatics* 12, 323.
- Liaw, A., and Wiener, M. (2002). Classification and Regression by randomForest. *R News* 2, 18–22.
- Love, M.I., Huber, W., and Anders, S. (2014). Moderated estimation of fold change and dispersion for RNA-seq data with DESeq2. *Genome Biol.* 15, 550.
- Maier, T., Guell, M., and Serrano, L. (2009). Correlation of mRNA and protein in complex biological samples. *FEBS Lett.* 583, 3966–3973.
- Mattison, J.A., Colman, R.J., Beasley, T.M., Allison, D.B., Kemnitz, J.W., Roth, G.S., Ingram, D.K., Weindruch, R., de Cabo, R., and Anderson, R.M. (2017). Caloric restriction improves health and survival of rhesus monkeys. *Nat. Commun.* 8, 14063.
- McCay, C.M., Crowell, M.F., and Maynard, L.A. (1935). The effect of retarded growth upon the length of life span and upon the ultimate body size. *Nutrition* 5, 155–171, discussion 172.
- Mootha, V.K., Lindgren, C.M., Eriksson, K.F., Subramanian, A., Sihag, S., Lehar, J., Puigserver, P., Carlsson, E., Ridderstrale, M., Laurila, E., et al. (2003). PGC-1alpha-responsive genes involved in oxidative phosphorylation are coordinately downregulated in human diabetes. *Nat. Genet.* 34, 267–273.
- Moskvin, O.V., McIlwain, S., and Ong, I.M. (2014). CAMDA 2014: making sense of RNA-Seq data: from low-level processing to functional analysis. *Syst. Biomed.* 2, 31–40.
- Moskvin, O.V., McIlwain, S., and Ong, I.M. (2015). CAMDA 2014: making sense of RNA-seq data: from low-level processing to functional analysis. *Syst. Biomed.* 2, 31–40.

- Nesvizhskii, A.I., and Aebersold, R. (2005). Interpretation of shotgun proteomic data. *Mol. Cell Proteomics* 4, 1419–1440.
- Newman, J.C., and Verdin, E. (2014). Ketone bodies as signaling metabolites. *Trends Endocrinol. Metab.* 25, 42–52.
- Peng, X., Thierry-Mieg, J., Thierry-Mieg, D., Nishida, A., Pipes, L., Bozinovski, M., Thomas, M.J., Kelly, S., Weiss, J.M., Ravendran, M., et al. (2015). Tissue-specific transcriptome sequencing analysis expands the non-human primate reference transcriptome resource (NHPTR). *Nucleic Acids Res.* 43, D737–D742.
- Phanstiel, D.H., Brumbaugh, J., Wenger, C.D., Tian, S., Probasco, M.D., Bailey, D.J., Swaney, D.L., Tervo, M.A., Bolin, J.M., Ruotti, V., et al. (2011). Proteomic and phosphoproteomic comparison of human ES and iPS cells. *Nat. Methods* 8, 821–827.
- Plank, M., Wuttke, D., van Dam, S., Clarke, S.A., and de Magalhaes, J.P. (2012). A meta-analysis of caloric restriction gene expression profiles to infer common signatures and regulatory mechanisms. *Mol. Biosyst.* 8, 1339–1349.
- Roberts, M.N., Wallace, M.A., Tomilov, A.A., Zhou, Z., Marcotte, G.R., Tran, D., Perez, G., Gutierrez-Casado, E., Koike, S., Knotts, T.A., et al. (2017). A ketogenic diet extends longevity and healthspan in adult mice. *Cell Metab.* 26, 539–546.e5.
- Rodriguez, S.A., Grochova, D., McKenna, T., Borate, B., Trivedi, N.S., Erdos, M.R., and Eriksson, M. (2016). Global genome splicing analysis reveals an increased number of alternatively spliced genes with aging. *Aging Cell* 15, 267–278.
- Schneider, A., Dahabi, J.M., Atamna, H., Clark, J.P., Colman, R.J., and Anderson, R.M. (2017). Caloric restriction impacts plasma microRNAs in rhesus monkeys. *Aging Cell* 16, 1200–1203.
- Subramanian, A., Tamayo, P., Mootha, V.K., Mukherjee, S., Ebert, B.L., Gillette, M.A., Paulovich, A., Pomeroy, S.L., Golub, T.R., Lander, E.S., et al. (2005). Gene set enrichment analysis: a knowledge-based approach for interpreting genome-wide expression profiles. *Proc. Natl. Acad. Sci. USA* 102, 15545–15550.
- Swindell, W.R. (2008). Comparative analysis of microarray data identifies common responses to caloric restriction among mouse tissues. *Mech. Ageing Dev.* 129, 138–153.
- Swindell, W.R. (2009). Genes and gene expression modules associated with caloric restriction and aging in the laboratory mouse. *BMC Genomics* 10, 585.
- Szklarczyk, D., Franceschini, A., Wyder, S., Forslund, K., Heller, D., Huerta-Cepas, J., Simonovic, M., Roth, A., Santos, A., Tsafou, K.P., et al. (2015). STRING v10: protein-protein interaction networks, integrated over the tree of life. *Nucleic Acids Res.* 43, D447–D452.
- Tyanova, S., Temu, T., Sinitcyn, P., Carlson, A., Hein, M.Y., Geiger, T., Mann, M., and Cox, J. (2016). The Perseus computational platform for comprehensive analysis of (proteo)omics data. *Nat. Methods* 13, 731–740.
- Wang, J., Duncan, D., Shi, Z., and Zhang, B. (2013). WEB-based GEne SeT AnaLysis Toolkit (WebGestalt): update 2013. *Nucleic Acids Res.* 41, W77–W83.
- Wang, T., Tsui, B., Kreisberg, J.F., Robertson, N.A., Gross, A.M., Yu, M.K., Carter, H., Brown-Borg, H.M., Adams, P.D., and Ideker, T. (2017). Epigenetic aging signatures in mice livers are slowed by dwarfism, calorie restriction and rapamycin treatment. *Genome Biol.* 18, 57.
- Wenger, C.D., Phanstiel, D.H., Lee, M.V., Bailey, D.J., and Coon, J.J. (2011). COMPASS: a suite of pre- and post-search proteomics software tools for OMSSA. *Proteomics* 11, 1064–1074.
- Wickham, H. (2017). *ggplot2-Elegant Graphics for Data Analysis* (Springer).
- Young, M.D., Wakefield, M.J., Smyth, G.K., and Oshlack, A. (2010). Gene ontology analysis for RNA-seq: accounting for selection bias. *Genome Biol.* 11, R14.
- Zimin, A.V., Cornish, A.S., Maudhoo, M.D., Gibbs, R.M., Zhang, X., Pandey, S., Meehan, D.T., Wipfler, K., Bosinger, S.E., Johnson, Z.P., et al. (2014). A new rhesus macaque assembly and annotation for next-generation sequencing analyses. *Biol. Direct* 9, 20.

STAR★METHODS**KEY RESOURCES TABLE**

REAGENT or RESOURCE	SOURCE	IDENTIFIER
Antibodies		
Rabbit anti-pan acetyl lysine	ImmuneChem	ICP-0388
Chemicals, Peptides, and Recombinant Proteins		
Sequencing grade trypsin	Promega	V5113
TMT 8 plex (from 10 plex kit)	Pierce	90110
Critical Commercial Assays		
BCA assay	Pierce	23225
Illumina TruSeq RNA sample prep kit	Illumina	RS-122-2001
Agilent DNA 1000 series chip assay	Agilent Genomics	5067-1504
Invitrogen Qubit HS kit	Fisher	Q32851
TruSeq Paired End Cluster Kit (v3)	Illumina	PE-401-3001
TruSeq 100 bp SBS kit	Illumina	FC-401-3001
Deposited Data		
Raw and analyzed RNA-seq data	This paper	GEO: GSE104234
Raw and analyzed proteomics data	This paper and Mendeley Data	Table S5; https://doi.org/10.17632/z4cttg3gp3.1
Rhesus macaque reference genome MacraM_Assembly_v7	Zimin et al., 2014	https://www.ncbi.nlm.nih.gov/assembly/GCA_000772875.1/
Experimental Models: Organisms/Strains		
Non-human primate: <i>Macaca mulatta</i>	Wisconsin National Primate Research Center	Colman et al., 2009
Oligonucleotides		
Primers for PCR validation of DEXseq exon changes, see Table S4	This paper	N/A
Software and Algorithms		
Chenomx NMR Suite v. 8.2	Chenomx	https://www.chenomx.com/software/
COLMAR	Bingol et al., 2015	http://spin.ccic.ohio-state.edu/index.php/colmar
TopSpin v. 3.5	Bruker	https://www.bruker.com/products/mr/nmr/nmr-software/software/topspin/overview.html
LipidBlast spectral library	Kind et al., 2013	http://fiehnlab.ucdavis.edu/projects/LipidBlast
COMPASS	Wenger et al., 2011	
STAR aligner	Dobin et al., 2013	https://github.com/alexdobin/STAR
RSEM	Li and Dewey, 2011	https://deweylab.github.io/RSEM/
DESeq2	Love et al., 2014	https://bioconductor.org/packages/release/bioc/html/DESeq2.html
GSEA	Mootha et al., 2003	http://software.broadinstitute.org/gsea/index.jsp
EBSeq	Leng et al., 2013	https://bioconductor.org/packages/release/bioc/html/EBSeq.html
DEXseq	Anders et al., 2012	https://bioconductor.org/packages/release/bioc/html/DEXSeq.html
Perseus	Cox and Mann, 2012	http://www.biochem.mpg.de/5111810/perseus
lme4	Bates et al., 2015	https://cran.r-project.org/web/packages/lme4/index.html
ggplot2	Wickham, 2017	http://ggplot2.org/
GoSeq	Young et al., 2010	https://bioconductor.org/packages/release/bioc/html/goseq.html
WebGestalt	Wang et al., 2013	http://webgestalt.org/option.php
randomForest	Liaw and Wiener, 2002	https://cran.r-project.org/web/packages/randomForest/index.html

CONTACT FOR REAGENT AND RESOURCE SHARING

Further information and requests for resources and reagents should be directed to Lead Contact Dr. Rozalyn Anderson (rmanderson5@wisc.edu).

EXPERIMENTAL MODEL AND SUBJECT DETAILS

This study was a retrospective analysis of previously harvested and banked biopsy tissue specimens collected from a subset of animals associated with a long-term study of caloric restriction in non-human primate rhesus monkeys (*Macaca mulatta*). Animals were born and lived their entire life at the Wisconsin National Primate Research Center (WNPRC), and therefore have known birthdates. Animals were adults, between 7 and 14 years of age, when they were enrolled in the study. Animals were fed a semi-purified, nutritionally fortified, low fat diet containing 15% protein and 10% fat. As part of the study design, animals were treated for presenting conditions. At the outset of that study, animals were randomized to Control or CR diets matching for sex, bodyweight, age, and baseline food intake, as described previously. The restricted diet was implemented gradually to reach 30% restriction for the CR group based on the individual baseline food intake. Liver biopsies were collected only twice during the study from a defined subset of male animals, at study enrollment and after two years of the diet regimen, frozen in liquid nitrogen and stored at -80 °C until use. All animal procedures were performed at the WNPRC under approved protocols from the Institutional Animal Care and Use Committee of the Graduate School of the University of Wisconsin, Madison. Biopsy specimens were coded before providing to collaborators. Researchers and technical staff charged with generating the molecular profiles were blind to the animal's diet group assignation and to the year at which the specimen was collected. Metabolite and lipid analyses were performed on biopsy samples from 11 animals (n=5 Control, n=6 CR). For transcriptomics analysis, samples from 10 animals were used (n = 5, both groups). For proteome and acetyl-proteome, samples from 8 animals were used (n = 4, both groups).

METHOD DETAILS

Metabolomics

Liver samples were dried in a speedvac overnight and then homogenized in PBS (pH 7.4) using an Omni International bead homogenizer unit at 6.45m/s for 30 sec. The homogenate was extracted with CHCl₃:MeOH (2:1) to separate polar and nonpolar metabolites. Samples were centrifuged at 3000 rpm for 5 min. For NMR metabolomics, the aqueous layer was dried in a speedvac overnight and resuspended in 150 mM phosphate buffer in 99.9% D₂O, pH 7.4, 0.04% NaN₃, and 100 μM 4,4-dimethyl-4-silapentane-1-sulfonic acid (DSS) as a chemical shift reference. The CHCl₃ layer was evaporated under nitrogen and resuspended in acetonitrile (ACN):isopropanol (IPA) 1:1, stored at -20 °C, and reserved for lipidomics analysis.

The NMR spectra were collected on a Bruker BioSpin Avance III 600 MHz spectrometer equipped with a 5 mm cryoprobe and a SampleJet sample changer. NMRbot was used to automate the data collection process (Clos et al., 2013). One-dimensional (1D) ¹H spectra were collected for all samples using a Carr-Purcell-Meiboom-Gill pulse sequence with f₁ presaturation, from 64 averaged transients consisting of 65,536 time-domain points with a sweep width of 12 ppm. Two-dimensional (2D) ¹H-¹³C Heteronuclear Single Quantum Coherence Spectroscopy (HSQC) spectra were collected using an Echo/Antiecho-TPPI (time-proportional phase incrementation) pulse sequence, from 8 transients consisting of 2,048 time-domain points with 256 increments in the indirect dimension, and a 2 s relaxation delay. 2D ¹H-¹H TOtal Correlation Spectroscopy (TOCSY) spectra were collected on representative samples using an MLEV17 pulse sequence, from 64 averaged transients consisting of 2,048 time-domain points with 256 increments in the indirect dimension, and a 2 s relaxation delay. All 2D spectra were collected with a ¹H spectral width of 11 ppm and 160 ppm for ¹³C. All data collection occurred at 25 °C.

To obtain the initial working set of metabolite identifications and quantifications, the 1D ¹H NMR spectra were phased, baseline corrected, and referenced to DSS using the Chenomx NMR suite 8.2. We then used Chenomx to manually fit spectral peaks corresponding to each individual candidate compound to the spectrum of the liver extract. We used 2D ¹H-¹H TOCSY spectra and ¹H-¹³C HSQC spectra to validate the identities of the key metabolites, both manually using TopSpin 3.5, and using the COLMAR software (Bingol et al., 2015).

Lipidomics

Rhesus liver extracts were thawed on ice and vortexed to mix. 10 μL of each extract was diluted with 1:1 ACN:IPA prior to analysis via liquid chromatography-tandem mass spectrometry (LC-MS/MS). LC-MS/MS analysis was performed on an Acquity CSH C18 column held at 50 °C (2.1 x 100 mm x 1.7 μm particle size; Waters, Milford, MA) using an Ultimate 3000 RSLC Binary Pump (400 μL/min; Thermo Scientific, San Jose, CA). Mobile phase A consisted of 10 mM ammonium acetate in ACN:H₂O (70:30, vol/vol) containing 250 μL/L acetic acid. Mobile phase B consisted of 10 mM ammonium acetate in IPA:ACN (90:10, vol/vol) with the same additives. Initially, mobile phase B was held at 2% for 2 min and then increased to 30% over 3 min. Mobile phase B was then further increased to 85% over 14 min and then raised to 99% over 1 min and held for 7 min. The column was then re-equilibrated for 5 min before the next injection. Ten microliters of lipid extract were injected by an Ultimate 3000 RSLC autosampler (Thermo Scientific, San Jose, CA). The LC system was coupled to a Q Exactive Focus mass spectrometer by a HESI II heated ESI source (Thermo Scientific, San Jose, CA). The MS was operated in polarity switching mode acquiring positive and negative mode MS¹ and MS² spectra (Top2) during the

same separation. MS acquisition parameters were as follows: 17,500 resolving power, 1×10^6 automatic gain control (AGC) target for MS¹ and 1×10^5 AGC target for MS² scans, 25 units of sheath gas and 10 units of auxiliary gas, 300 °C HESI II and inlet capillary temperature, 100-ms MS¹ and 50-ms MS² ion accumulation time, 200- to 1,600-Th MS¹ scan range, 1-Th isolation width for fragmentation, stepped HCD collision energy (20, 30, 40 units), 1.0% under fill ratio, and 10-s dynamic exclusion.

Individual lipid species were identified by searching the discovery LC-MS/MS data against the LipidBlast in-silico lipid spectral library (Kind et al., 2013) with a precursor and product ion tolerance of 0.01 Th. Spectral matches with dot products below 500 were not considered. Matching spectra were manually inspected to ensure proper identification. Lipid quantification was performed by extracting the apex MS¹ signal for each identified lipid species. Total lipids were normalized to the summed intensity, with z-score normalization and log₂ transformation performed on individual lipid classes: glycerolipids, phosphoglycerolipids, and fatty acids.

Proteomics and Acetyl-Proteomics

Liver samples were homogenized with 3 strokes of a motorized stirrer at 1500 rpm in a Potter-Elvehjem tissue grinder with 1 mL of buffer (8 M urea, 50 mM Tris pH 8.0, 1 mM CaCl₂, 100 mM NaCl, protease inhibitor cocktail from Roche, and deacetylase inhibitors—nicotinamide and sodium butyrate). Homogenates were then sonicated at 5 W for 30 seconds and centrifuged at 10,000xg for 5 mins to clear the lysate of debris. Lysates were stored at -80 °C until analysis.

Total protein content was quantified by the Bicinchoninic acid assay (Pierce, Rockford, IL). Two milligrams of total protein from each liver lysate was reduced and alkylated (5 mM DTT at 37 °C for 30 min, followed by 15 mM iodoacetamide at RT for 30 min), then diluted 5-fold with 50 mM Tris pH 8.0, 100 mM NaCl, and 5 mM CaCl₂. The samples were then digested with trypsin (Promega, Madison, WI) overnight at ambient temperature (1:50 w/w trypsin:protein ratio). The digestions were quenched by acidification with TFA to 0.5% and desalting with a tC18 sep-Pak (Waters, Milford, MA). Samples were divided into two 8-plex TMT (Pierce, Rockford, IL) experiments and labeled according to the manufacturer's instructions. Experiment 1 contained animals 001, 004, 005, and 007, while experiment 2 contained 006, 008, 009, and 011. Tagged samples were combined in equal ratios and desalting as before.

Samples were fractionated using strong cation exchange (SCX) on a polysulfoethyl A column (9.4 mm x 200 mm; PolyLC). Ten fractions were collected per replicate, dried in a Speed-Vac, and desalting. An aliquot (5% of total volume) of each fraction was set aside for protein abundance measurements. The remainder of the SCX fractions were concatenated to four fractions for acetyl-lysine enrichment and dried in a Speed-Vac. Each fraction was dissolved in 1 mL of enrichment buffer (50 mM HEPES pH 7.5, 100 mM KCl). Pan-acetyl lysine antibody-agarose conjugate (50 μL, Immunechem, Burnaby, BC, Canada) was added to each fraction, and the samples were rotated overnight at 4 °C. The beads were rinsed eight times with buffer, and acetyl-lysine peptides were eluted via incubation with 0.1% TFA for 30 minutes. Eluted peptides were desalting prior to analysis.

All peptide fractions were analyzed by reversed phase liquid chromatography on a nanoAcquity LC (Waters) coupled to an LTQ-Orbitrap Elite (Thermo, San Jose, CA). Samples were loaded onto a 75 μm inner diameter column packed with 1.7 um BEH C₁₈ particles (Waters, Milford, MA). The elution portion of the gradient was 4% to 25% B (A: water/0.2% formic acid; B: acetonitrile/0.2% formic acid) over 80 minutes. Mass spectrometry data were collected using data-dependent acquisition (DDA), consisting of a single MS¹ survey scan (resolution = 60,000; 350 Th – 1,300 Th) followed by data-dependent MS² fragmentation and analysis (resolution = 30,000) of the fifteen most intense precursors.

Raw mass spectrometry data were processed using the COMPASS suite (Wenger et al., 2011). Spectra were converted to searchable text files using DTA generator and searched against a concatenated target-decoy protein sequence database, constructed from the aligned RNA transcripts, using the OMSSA algorithm (Geer et al., 2004). Three missed cleavages were allowed, and carbamido-methylation (+57.021464) of cysteine, TMT 6plex on lysine (+229.162932), and TMT 6plex on peptide N terminus (+229.162932) were searched as fixed modifications for all samples. Methionine oxidation (+15.994915) and TMT 6plex on tyrosine (+229.162932) were searched as variable modifications for all samples. Enriched fractions were additionally searched for variable acetylation modifications. In this case, the acetylation mass shift was set to -187.1523 Da, the difference between an acetyl group and a TMT 6plex tag. Using this custom mass shift allows TMT 6plex on lysine to remain as a fixed modification even for acetylated peptides. Search results were filtered to 1% FDR at the unique peptide level. TMT quantification of identified peptides was performed within COMPASS as previously described (Phanstiel et al., 2011). Peptides were grouped into proteins according to previously reported rules of parsimony and protein identifications were further filtered to 1% FDR (Nesvizhskii and Aebersold, 2005). Protein quantification was performed by summing all reporter ion intensities within each channel for each protein. Peptides in multiple protein groups were excluded from quantitation, and at least two peptides were required for quantification. Data from the two TMT experiments was combined after mean normalizing reporter ion intensities across each protein and then matching the unique Protein Group Identifier.

Acetylation events were localized to specific residues using probabilistic methods described elsewhere (Kim et al., 2011). Briefly, for each peptide spectral match (PSM) that contains an acetyl modification, every possible peptide isoform was generated and fragmented in silico to produce theoretical fragmentation spectra. Each theoretical spectrum was compared to the experimental spectrum at 10 PPM m/z tolerances; the number of matching peaks was recorded and a p value was calculated using a cumulative binomial distribution. An AScore (i.e., the difference of p values) was calculated between every pair of isoforms. A peptide was declared “localized” if all AScores for a particular isoform were larger than the minimum value (AScore = 13, p value < 0.05) for every comparison. Localized acetylated peptides were grouped together if they share identical modification sites and the reporter ion intensities were summed; peptides with C-terminal acetylation are excluded from quantitation. The term ‘acetyl sites’ refers to individual

acetylation marks; the term ‘acetyl proteoform’ indicates an acetylation pattern, which can include multiple sites, from a peptide. Acetyl proteoforms with multiple sites use the ‘|’ character to separate the sites (e.g., K267|K273).

Transcriptomics

Liver samples were homogenized in 1 mL TRIzol per 50 mg wet weight. Manual grinding with a pestle was used to pulverize the tissue, following which the sample was incubated for 5 min at room temperature. RNA extraction proceeded using a Direct-zol RNA kit (Zymo Research, Irvine, CA) according to the manufacturer’s instructions. RNA was then submitted to the University of Wisconsin-Madison Biotechnology Center Sequencing Facility for high throughput RNA-seq.

Each RNA library is generated following Illumina “TruSeq RNA Sample Preparation Guide and the Illumina TruSeq RNA Sample Preparation Kit (Illumina, San Diego, California, USA). Quality and quantity of finished libraries are assessed using an Agilent DNA1000 series chip assay (Agilent Technologies, Santa Clara, CA) and Invitrogen Qubit HS Kit (Invitrogen, Carlsbad, California, USA), respectively. Each library is standardized to 2 μ M. Cluster generation is performed using a TruSeq Paired End Cluster Kit (v3) and the Illumina cBot, with libraries multiplexed for 2x100bp sequencing using the TruSeq 100bp SBS kit (v3) on an Illumina HiSeq2000. Images are analyzed using CASAVA 1.8.2.

Sequencing reads were trimmed using the Skewer trimming program to remove sequencing adapters and bases with quality scores lower than Q20 (Jiang et al., 2014). Trimmed reads were subsequently aligned to the *Macaca mulatta* reference genome (Zimin et al., 2014) using the STAR aligner (Dobin et al., 2013). Quantification of expected read counts for each gene and isoform was calculated by RSEM (Li and Dewey, 2011). Transcripts were removed from the analysis if they had fewer than 5 reads in half of the samples. The remaining read counts were used for differential gene expression analysis using DESeq2 (Love et al., 2014), with the results used for pathway analysis via GSEA (Mootha et al., 2003; Subramanian et al., 2005). To further filter transcripts that were not changing between Control and CR, we calculated the critical coefficient (crt) (Moskvin et al., 2014) for each gene, which is a ratio of the lowest individual replicate value, of the condition whose average signal (across all biological replicates) is greater, to the highest replicate value of the condition whose average signal is smaller. A large crt value indicates a more consistent separation of the gene’s replicate measurements between the two conditions (Control and CR). It is defined as:

$$crt(gene) = \begin{cases} mean(condA_{gene}) \geq mean(condB_{gene}), \frac{\min(condA_{gene})}{\max(condB_{gene})} \\ mean(condA_{gene}) < mean(condB_{gene}), \frac{\min(condB_{gene})}{\max(condA_{gene})} \end{cases}$$

where genes were only kept for further differential expression analysis if the crt value of the longitudinal difference between the two conditions, calculated from median normalized values using EBSeq (Leng et al., 2013), was above 0.7. Differential exon usage was performed using DEXseq (Anders et al., 2012) (v. 1.16.10) on exon feature counts generated by HTSeq (Anders et al., 2015) (v. 0.6.1p1).

Five exon changes identified by DEXseq were selected for validation via polymerase chain reaction (PCR); in selecting these genes, we were guided by gene architecture, expression level and degree of fold change calculated by DEXseq, and feasibility of primer design. The high-capacity cDNA Reverse Transcription Kit (ThermoFisher #4368814) was used to produce cDNA from 1 μ g of total RNA extracted from rhesus macaque liver tissue, according to the manufacturer’s instructions. The cDNA was diluted 1:4 with water, and 3 μ L of diluted cDNA was used as the template for PCR (New England Biolabs #M0273S), which was run according to the manufacturer’s specifications. Following PCR amplification, products were analyzed via a 1.3% agarose gel (containing 83.3 ng/mL ethidium bromide), which was visualized using a UV transilluminator.

Data Analysis

Non-RNA Data normalization was performed in, and heat maps were generated in, Perseus (Cox and Mann, 2012; Tyanova et al., 2016) (v. 1.5.5.3). Linear mixed-model analysis of metabolomics data and regression analysis of biometrics-metabolite interactions were performed in RStudio (v. 0.99.903; R v. 3.3.1) using the lme4 (Bates et al., 2015) and ggplot2 (Wickham, 2017) packages. String analysis used only high confidence interactions (> 0.700), and were based on data sources including Experiments, Database, Co-expression, Gene Fusion, and Co-occurrence.

Pathway analysis was performed using either GoSeq (exon changes, cluster membership) (Young et al., 2010), WebGestalt (significant proteins and acetyl proteoforms) (Wang et al., 2013), or Gene Set Enrichment Analysis (GSEA) (all other analyses). The GSEA was performed using the *xtools.gsea.GseaPreranked* program from the GSEA java package (Mootha et al., 2003; Subramanian et al., 2005). For each gene, protein, and acetylation proteoform a score was generated using the function $Score(Molecule_i) = sign(\log_2Fold-Change)_i/pvalue_i$, and the gene sets were compiled from the latest version of KEGG (Kanehisa et al., 2017) (human). Results were generated separately for the gene, protein, and acetylation datasets using their respective gene identifications. Biomart (Durinck et al., 2005) was used to convert the gene symbols to entrez ids; their associated KEGG ids and missing ids were manually assigned using NCBI homologene (<https://www.ncbi.nlm.nih.gov/homologene>).

Data Integration

All data were Z-scaled by molecule (Gene, Protein, Acetylation, Lipid, and Metabolite) and concatenated into one matrix. Pearson correlations between all molecules were calculated from just the CR 2yr-0yr (A), Control 2yr-0yr (B), CR and Control 0yr (C), and all samples (D) using the Z-scale values (See Biomarker Discovery). Complete hierarchical clustering was used to reorder the columns and rows using $1 - \text{cor}(\text{Molecule}_i, \text{Molecule}_j)$ as the distance metric. For unbiased cluster membership analysis, correlation coefficient cut-offs to define clusters were determined based on the n value and the corresponding Pearson p value for 0.05 based on a t test. Mega-cluster groupings were then assigned manually. For each mega-cluster, we determined the over representation of the KEGG (Kanehisa et al., 2017) pathways from the included gene, protein, and acetylation using goseq (Young et al., 2010).

Random forest classifiers were generated for each of the gene, protein, and acetyl datasets using the *randomForest* package in R (Liaw and Wiener, 2002). The number of trees generated for each classifier was capped at 8000, as increasing beyond that point did not change the outcome. Each tree is constructed using a different bootstrap sample from the original data, selected with replacement. The remaining samples that are left out of the construction of a given tree comprise the test set against which the tree is evaluated, so-called out-of-bag error calculation. To calculate variable importance, each variable (molecule) is randomly permuted in the out-of-bag cases and compared to the unpermuted version; the difference between these numbers, averaged over all of the trees in the classifier, is the importance score (or mean decrease accuracy). Every time a split of a node is made on a variable, the gini impurity criterion for the two descendent nodes is less than the parent node. Adding up the gini decreases for each individual variable over all trees in the forest yields the mean decrease gini score.

QUANTIFICATION AND STATISTICAL ANALYSIS

T tests were two-tailed. Statistical significance of linear mixed-model analysis was assessed using a Wald test from the car (Fox and Weisberg, 2011) package.

DATA AND SOFTWARE AVAILABILITY

RNA-seq data have been deposited with the Geo repository (GSE104234). Raw and processed proteomics data are hosted on Men-deley data (<https://doi.org/10.17632/z4cttg3gp3.1>). All other data available upon request.